The femtosecond laser induced $Zr_{64.13}Cu_{15.75}Ni_{10.12}Al_{10}$ amorphous periodic surface structure

Junzhe Wang[a,b], Peilei Zhang[a,b,c*], Lei Shen[a,b], Zhishui Yu[a,b,], Haichuan Shi[a,b], Yingtao Tian[d]

[a]School of Materials Engineering, Shanghai University of Engineering Science, Shanghai 201620, China

[b]Shanghai Collaborative Innovation Center of Laser of Manufacturing Technology, Shanghai 201620, China

[c]Fraunhofer Institute for Laser Technology ILT, Aachen 52074, Germany

[d]Department of Engineering, Lancaster University, Lancaster LA1 4YW, United Kingdom

Abstract

We reported femtosecond laser-induced self-organized micro/nanostructures on $Zr_{64.13}Cu_{15.75}Ni_{10.12}Al_{10}$ amorphous surfaces. A set of process methods that induced sub-wavelength LIPSS(Laser-induced periodic surface structures) structures and SWPSS (super-wavelength periodic structure) nearly twice the wavelength using 1030 nm wavelengths were observed. Using linear scanning can completely cover a layer of micro/nanostructures on the surface. Clear surface structures can be observed throughout the laser ablation area, and their cycles and structural fluctuations can be controlled by process parameters. The causes and structures of the two micro/nanostructures were discussed.

1. Introduction

The amorphous alloy was a new kind of material with high tensile strength, excellent hardness, and great corrosion resistance[1–3]. In recent decades, it has been widely concerned by

---

* Corresponding authors: Peilei Zhang (peilei@sues.edu.cn) and Zhishui Yu (yu_zhishui@163.com)

researchers, and in medical, precision instruments, and other applications[4–6]. Amorphous alloys need a high degree of supercooling from the molten state to the solid state, so most of them use suspension melting-copper mold suction casting[7]. Zr-based amorphous alloys have good amorphous forming capabilities and a very wide supercooled liquid area[7]. At the same time, Zr-based amorphous have matching biological bone strength and good bio-compatibleness[8]. As a new human implant material, Zr-based amorphous has a very high elastic strain capacity and relatively close to the elastic mod of human bone[9], the lower elastic mod can effectively disperse the load, reduce the stress shielding effect, promote bone tissue healing. However, a smooth surface was difficult to promote cell adsorption[6]. Laser processing micro/nano structures on amorphous surface can significantly improve the adsorption capacity of biological cells on the surface of the material, thus increasing the biocompatibility of the material.

Femtosecond laser processing was a clean, non-contact, high-precision material processing method that enables material reduction and surface micro/nanostructures processing without crystallizing[10,11]. Because the instantaneous fluence of the femtosecond laser was very high, the material can be converted from solid to plasma in a very short time scale[10]. In addition, the femtosecond laser has a very short action time of about 10^{-15} seconds. The action time was much shorter than the minimum time for material heat transfer. As a result, the femtosecond laser produces a little thermal effect on the material[12]. This allows the femtosecond laser to achieve cold processing of the material. To improve the surface biocompatibility of $Zr_{64.13}Cu_{15.75}Ni_{10.12}Al_{10,}$ we use a femtosecond laser for periodic micro/nano structures processing.

Huang et al.[13] had studied the biocompatibility of Zr-based amorphous alloys as plastic surgery materials, conducted a series of biocompatibility tests, and explored the effects of added element Y and surface roughness on the behavior of osteoblasts. The experiment of culturing mouse osteoblast precursor cells (MC3T3-E1) on the surface of $Zr_{55}Al_{10}Cu_{30}Ni_5$ and $(Zr_{0.55}\text{-}Al_{0.10}Cu_{0.30}Ni_{0.05})_{99}Y1$ amorphous alloys showed that Zr-BMG was also found to have a positive effect on MC3T3-E1. The pre-osteocytes are non-toxic and exhibit biocompatibility comparable to Ti-6Al-4V alloy. Compared with smooth samples, all rough samples have higher ALP activity. The results of cell adhesion are related to SFE that affects protein adsorption. With the addition of a small amount of Y, the smooth surface cell behavior does not change significantly, while the ALP

activity of the rough surface with Y added is slightly reduced, but a certain roughness surface can improve the biocompatibility of the alloy surface.

Gaggl et al.[14] used aluminum alumina blasting, hydrofluoric acid corrosion, plasma spraying, and laser treatment to rough the surface of the implant titanium treatment. By contrast, it was found that laser processing is a new method for processing the surface of implants to produce high purity titanium oxide, and has enough roughness to achieve good bone integration, although the study did not validate organisms.

C.L. Qiu[9] et al. studied the amorphous biological properties of the cast $Zr_{60}Cu_{22.5}Pd_5Al_{7.5}Nb_5$. The material has excellent corrosion resistance in the human body fluid environment and does not separate harmful substances. The potential cytotoxicity was observed by culturing cells with BMG (Bulk metallic glass) for one week by the MTT method. The results show that the $Zr_{60}Cu_{22.5}Pd_5Al_{7.5}Nb_5$ has better biological properties than the traditional implant Ti-6Al-4V.

Alberto Jorge-Mora[15] et al. have studied the biological effects of laser-induced periodic surface structures (LIPSS) on tantalum and titanium materials. The laser energy selected for the experiment was near the damage threshold of titanium and tantalum. The article proves that compared with smooth surfaces, surface microtextures can effectively increase the osteogenic differentiation of human bone marrow stem cells cultured in vitro on titanium and tantalum surfaces. At the same time, the presence of LIPSS did not increase the inflammatory response of cells. LIPSS modification leads to a significant increase in cell metabolism. Similar improvements were observed in the inflammatory response to substances (IL-6 and TNF-alfa values).

At present, it has been proved that the amorphous materials' surface with micro textures has excellent biocompatibility. As a human implant, it has great potential. The effects of different surface fabrics on biological properties were not yet known. In this paper, the periodic texture of the amorphous surface was induced by adjusting some experimental parameters. Two kinds of stable and uniform surface micro/nanostructures were produced. The connections between structure and parameters were clear and controllable. We record and characterize the relationship between morphology and parameters. The characteristics and formation mechanism of the fabric formed on the surface of $Zr_{64.13}Cu_{15.75}Ni_{10.12}Al_{10}$ under different parameters were studied.

2. Experimental equipment

2.1 Femtosecond laser test platform

The experiment uses the femtosecond processing experimental platform built by Amplitude company, and the experimental equipment used high-power femtosecond processing. The platform and the experimental equipment were composed of a high-precision scanning galvanometer and a high-power femtosecond laser, which can achieve large-area. High-precision surface processing. The experimental processing equipment is shown in Fig.1.
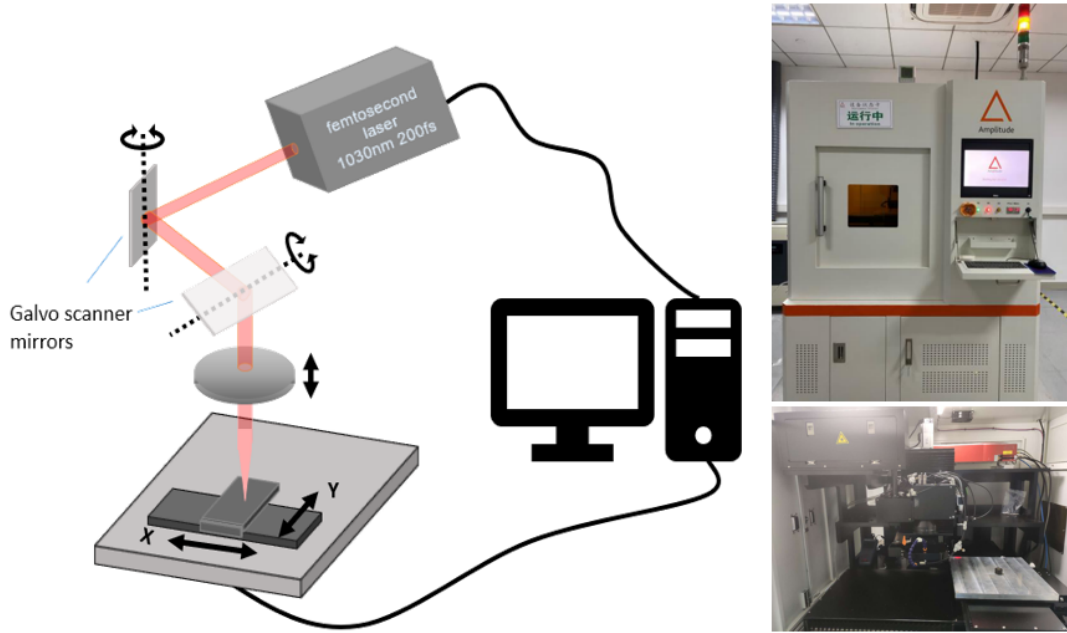

Fig.1 Femtosecond laser processing experimental platform

2.2 Test samples and parameters

The processing material used in this experiment was as-cast $Zr_{64.13}Cu_{15.75}Ni_{10.12}Al_{10}$ rod-shaped amorphous with a diameter of about $\phi3$ mm. Before the experiment, the cylindrical $Zr_{64.13}Cu_{15.75}Ni_{10.12}Al_{10}$ sample was cut into disc-shaped pieces with a thickness of about 1.5 mm and a diameter of 3mm with a wire-cut electric discharge machine. Use a hot setting machine to inlay a small amorphous piece on a thermosetting plastic sample with a diameter of 2 cm to facilitate subsequent processing. The inlaid samples were polished step by step with 600 #, 800 #, 1000 #, 2000 # sandpaper, and 2.5w # polishing paste was used to polish the nylon polishing cloth to a scratch-free mirror surface to avoid surface irregularities. The potential impact of leveling and scratches on experimental results. The polished sample was soaked in ethanol for 5minutes and then ultrasonically cleaned in ethanol to remove residual impurities on the polished sample. Blow-dry and seal the cleaned pattern and store it in a dry box for later use.

2.3 Test plan

Before use, wipe the prepared pattern with alcohol cotton to remove dust and impurities, and fix the pattern on the high-precision mobile platform of the femtosecond processing equipment with tape. Use the computer console to adjust the laser focus distance to focus the laser on the surface of the material, and ensure that the laser is vertically focused on the surface of the sample. The laser path was drawn in CAD, as shown in Fig 2, the distance between laser paths was 10 um, and the laser galvanometer scans the surface of the material according to the pre-drawn path.

2.4 Surface characterization equipment

2.4.1 Scanning Electron Microscope

Scanning electron microscope (SEM) is one of the most commonly used experimental equipment for observing the microstructure and characterization of materials. The main surface data of this article are obtained by scanning electron microscope (SEM). In scanning electron microscopy (SEM), a focused electron beam is used to scan the surface of the sample, and signals are collected by various detectors for chemical composition imaging and analysis (EDX).

2.4.2 Differential Scanning Calorimeter

The differential scanning calorimeter (DCS) uses software to control the heating temperature and speed. According to the principle of differential scanning calorimetry, when the material is in a constant temperature rising, falling, or constant temperature environment and a constant gas flow atmosphere, the material When the physical properties of the sample change (such as crystallization, melting, or material phase change), it is often accompanied by a change in the thermodynamics of the material. The software will measure the relationship between the temperature and time of the sample material.

A device that measures the laws of the physical properties of materials under temperature changes. Therefore, the horizontal axis of the curve obtained by DSC is the temperature (time), and the vertical axis is the heat difference. From the DSC chart, we can get the glass transition (Tg), melting temperature (Tm), and crystallization temperature (Tc) of the material.

Experimental parameters	Numerical
Energy density, s, J/cm^2	0.06 J/cm^2; 0.08 J/cm^2; 0.10 J/cm^2; 0.12 J/cm^2; 0.14 J/cm^2
Pulse repetition rate , f, kHz	10 kHz; 15 kHz; 20 kHz; 30 kHz; 40 kHz
Wavelength, λ, nm	1030 nm
The number of repetitions, N, times	5

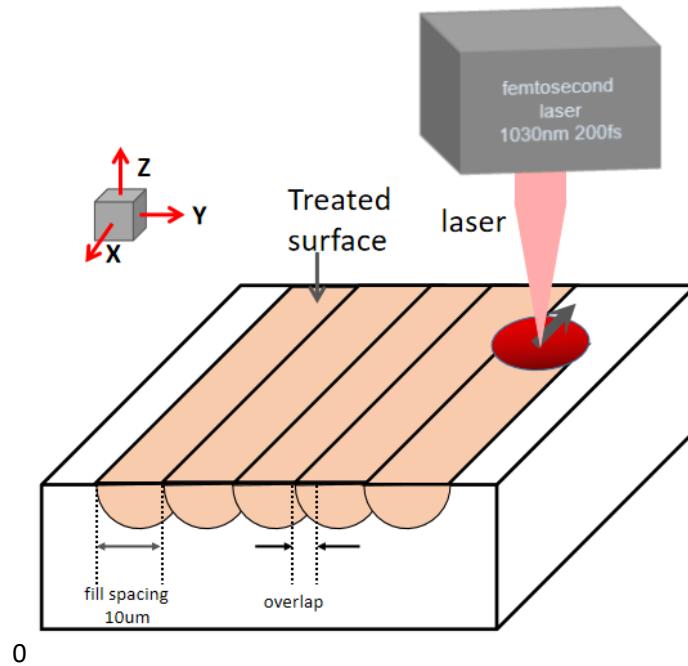Table 1. The parameters of the Femtosecond pulse laser experiment

Fig.2 Schematic diagram of the experimental laser path

3. Results and discussions

3.1 Analysis of the thermodynamic properties of the material

The results of the DSC study showed that the temperature of glass transformation and crystallization was measured at a heating rate of 20 K/min, as shown in Fig.3. The glass conversion temperature (T_g) was 394.4 ℃, crystallization temperature (Tx) was 405.2 ℃ and the heating peak temperature was 483.5 ℃. The DSC curve indicated an increase in the thermal capacity of amorphous alloys at the glassed transition temperature due to significant changes in dynamic viscosity and the transition of amorphous alloys to superplastic states. The glass transition temperature was consistent with the starting phase temperature of glass devitrification. At further heating, due to the crystallization of the over-cooled liquid, a subsequent sharp single peak heat release begins at the starting temperature (T) and the transition to crystallization was monitored by heat release. In general, the glass transition temperature of large amorphous alloys was lower than the crystallization temperature, while the difference between T_x and T_x- T_g determines the crystallization capacity of amorphous alloys [16].
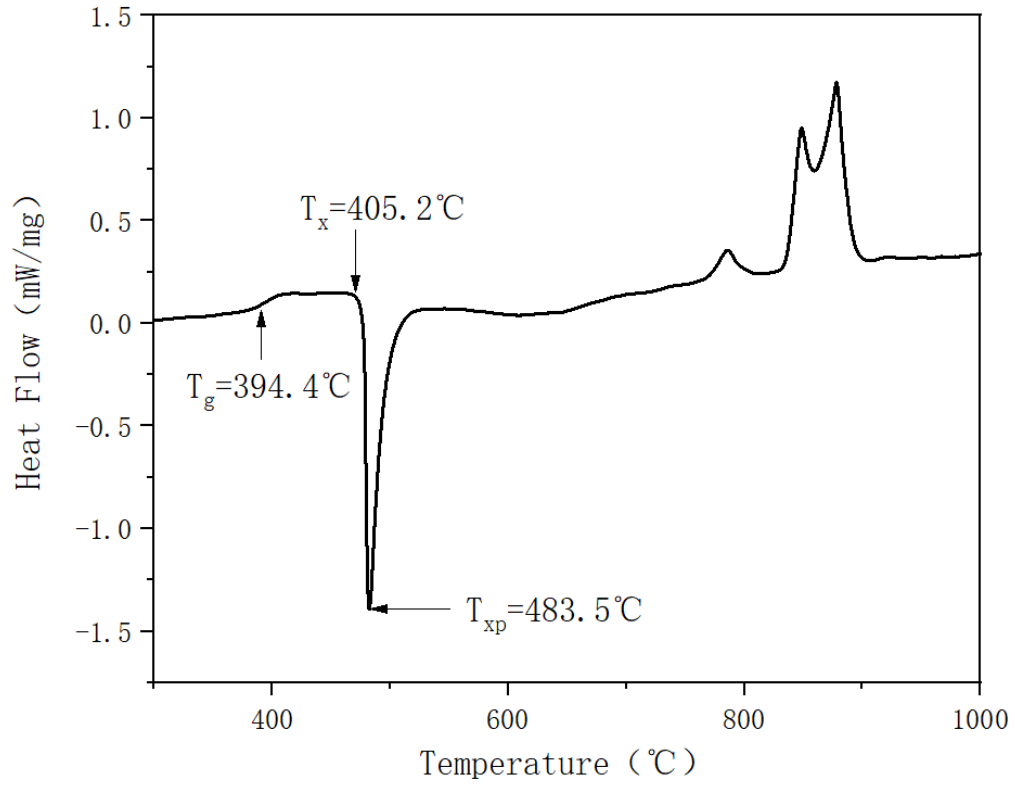
Fig.3 $Zr_{64.13}Cu_{15.75}Ni_{10.12}Al_{10}$ amorphous alloy melts and solidifies DSC curves at 20 K/min.

3.2 The influence of energy density

Fig.4 shown that the LIPSS periodic structure induced on the surface of the $Zr_{64.13}Cu_{15.75}Ni_{10.12}Al_{10}$ amorphous material at different energy densities and different frequencies. The scanning speed was 200 mm/s, the laser pulse width was 300 fs, the pulse width interval was 10um. Under different parameters, the surface of the material has changed to different degrees. Moreover, the surface morphology of the material will have a significant structural evolution as the energy density increased. These structures include fine particle structure, striped LIPSS structure, dot net structure, SWPSS structure.
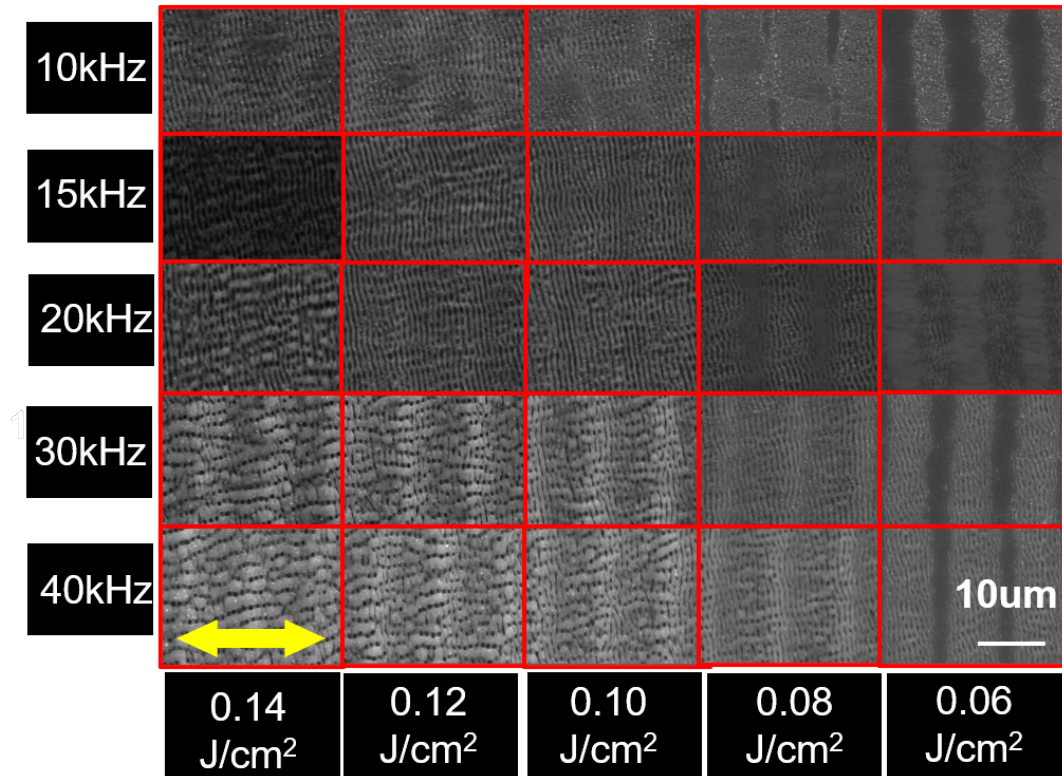
Fig.4 SEM images of the fabricated patterns arranged in terms of laser fluence (X-Axis) and repetition rate (Y-axis). The yellow arrow is the polarization direction.

At a repetition rate of 10 kHz, when the energy density was 0.06 J/cm^2, the material microstructures were shown in Fig.5A. At this time, the surface characteristic of the material was that the processing traces were distributed along the scanning direction, and the surface was evenly distributed with smaller granular protrusions. This kind of surface protrusion was spherical, similar to a drop shape. This special morphology was caused by the removal of the material after the surface of the material has absorbed a large amount of energy of the femtosecond laser in a very short time. Under the combined action of the reaction force of the plasma plume and the change in a surface temperature gradient, Marangoni convection (Marangoni convection) was caused, and finally, such surface protrusions are formed. Marangoni convection means that when the temperature changes along the target surface, the gradient of the surface tension also changes significantly. Thermal capillary forces were generated to transfer fluid from hot areas to cold areas. This phenomenon was called the Marangoni effect or capillary motion. Similar phenomena have also appeared on other metals and semiconductor materials[17]. It was mainly found in the parameters of low energy input and close to the ablation threshold and low laser repetition rate.

The area affected by ablation was narrower than the size of the laser spot (0.0125 mm), and the area without obvious ablation marks maintains the morphology of the raw material surface or only granular molten splash adheres. Since the energy of the laser had a Gaussian distribution, that was, the energy in the center of the spot was high and the energy was concentrated, and the energy of the spot was gradually attenuated to the outside. Therefore, the energy of the spot close to the outside was lower and was lower than the ablation threshold under the corresponding parameter under this energy input. The impact here was small, or even no impact, and the height was significantly higher than the central area of the path.
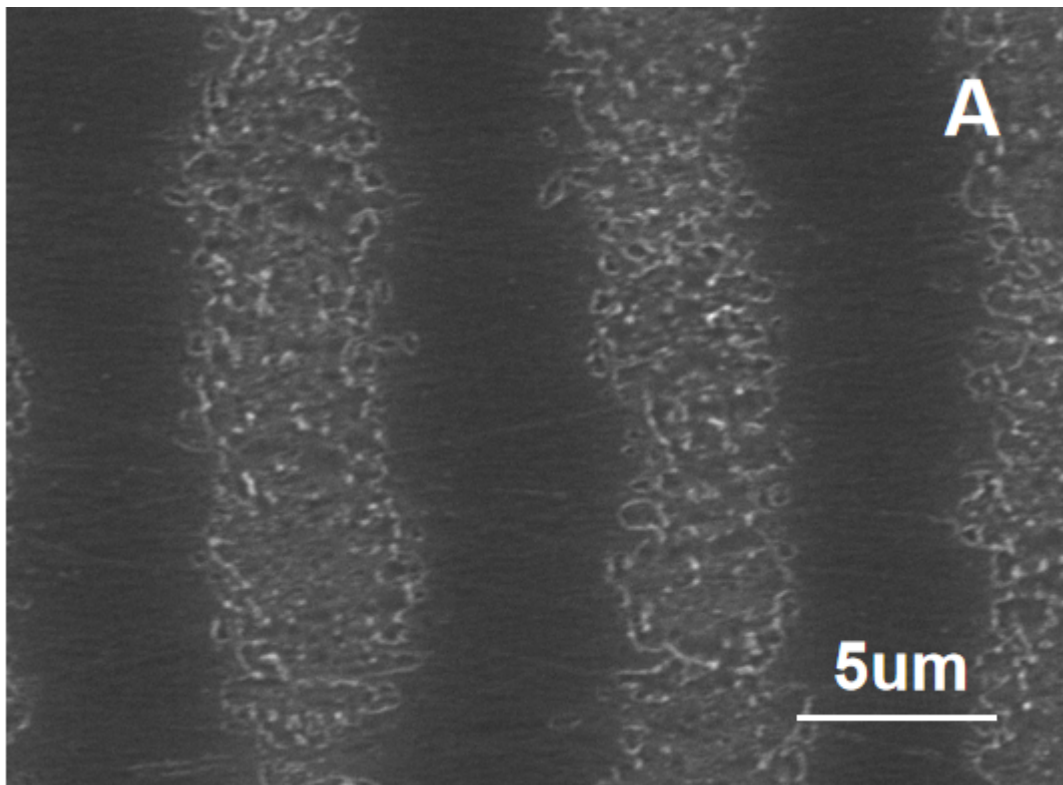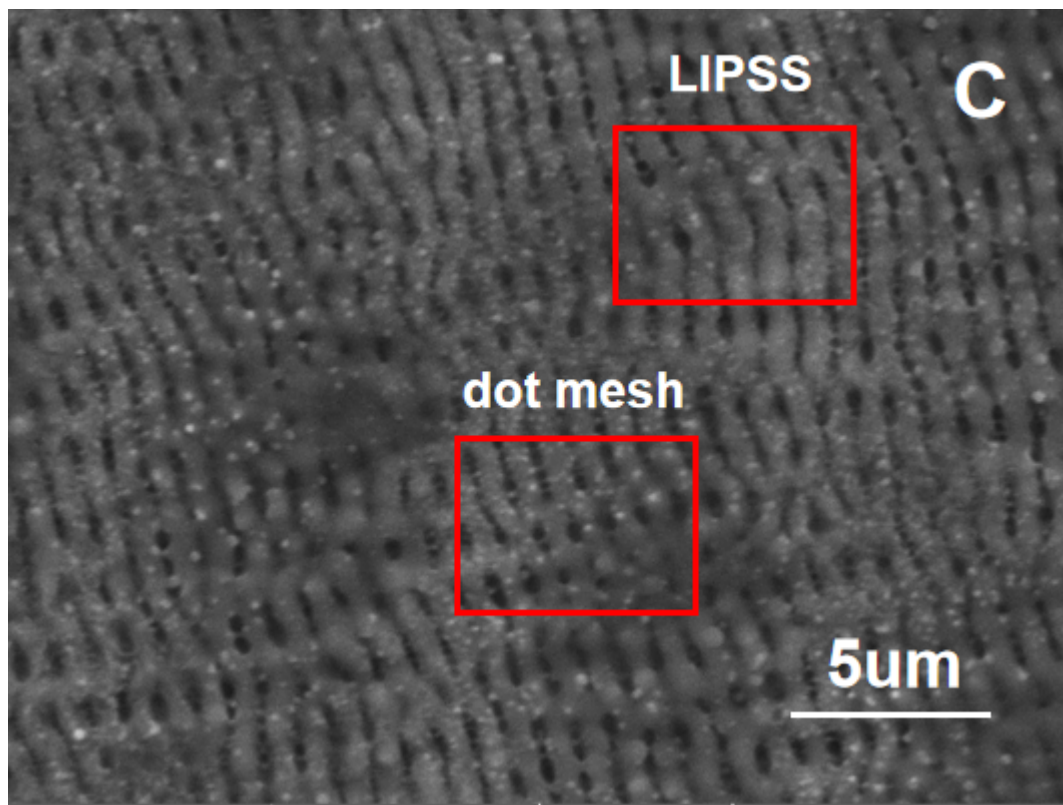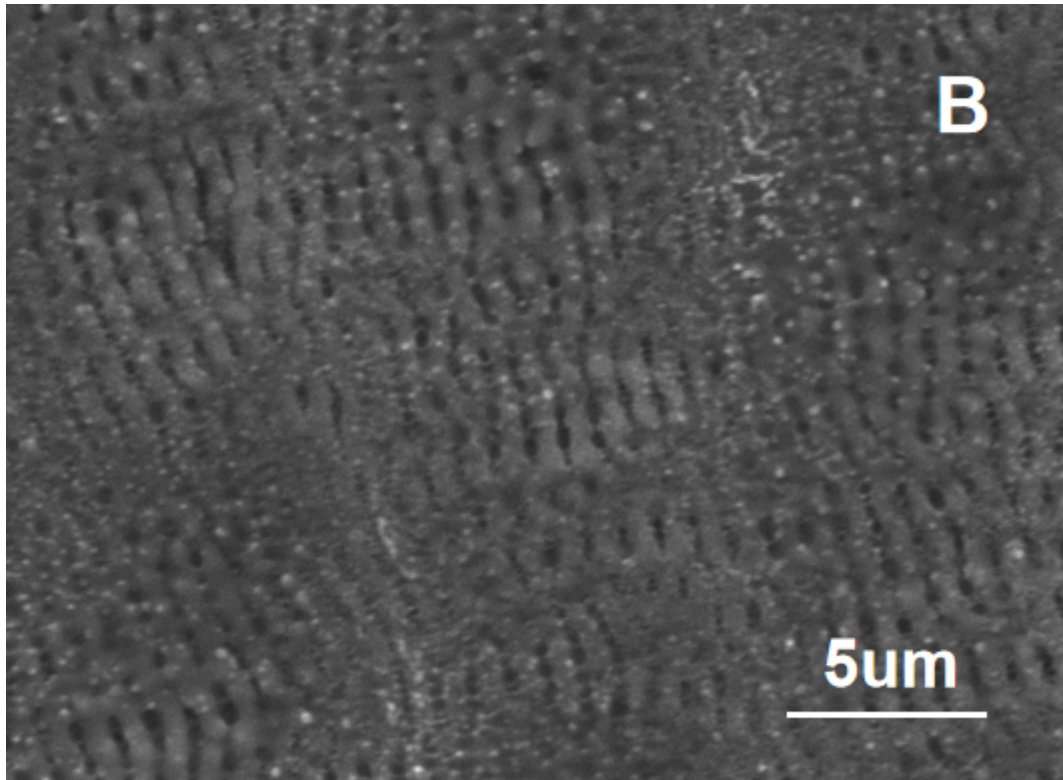
Fig.5 SEM images of different energy densities at 10 kHz repetition rate, the energy density of A was 0.06 J/cm^2, the energy density of B was 0.10 J/cm^2, and the energy density of C was 0.12 J/cm^2

When the energy density increased to 0.10 J/cm^2, as shown in Fig.5B. The surface of the material produced a clear, periodic striped structure, and the extension direction of this structure was perpendicular to the polarization direction of the laser. This structure was called LIPSS (laser-induced periodic surface structure). The LIPSS structure covered the entire surface of the material and had a certain depth. As the energy density of the femtosecond laser was further increased, the structure of LIPSS was gradually clear, and the amount of molten material on the surface of the material increased with the increase of the energy density.

When the repetition rate was 10 kHz and the energy density was 0.12 J/cm^2, the surface structure of the material was shown in Fig.5C. We found that the upper part of the LIPSS stripes became wider and connected to adjacent stripes to form a lateral structure perpendicular to the LIPSS. This horizontal structure also had a certain periodicity and formed a dot network structure with the existing LIPSS. This structure was distributed in a small number of areas on the surface of the material, and no clear relationship between its distribution position and the laser spot has been found.

At present, researchers generally believe that the formation of LIPSS was due to the interference between incident femtosecond laser radiation and surface electromagnetic waves generated by rough surfaces, which may include surface plasmons (SPP)[18]. The incident laser beam interfered electromagnetically on the surface. Waves were generated by surface plasmon polariton (SPP), resulting in spatial periodic energy distribution on the surface. Surface plasmon polaron (SPP) was an electromagnetic wave that propagates along with the metal-medium interface. It was the result of the interaction of conduction band electrons. Due to the mismatch of the photon momentum, the coupling of the surface plasmon and the incident laser beam usually does not occur, but the existence of periodic ripples or topological defects on the conductor surface will cause the coupling to occur. Generally, the first few pulses produced shallow, randomly distributed nanostructures on the surface of the material. These nanostructures promote the coupling of surface plasmons with the incident beam, enabling them to propagate on the interface. With the subsequent interference between the laser pulse and the surface plasma, the energy deposited on the surface became spatially non-uniform, resulting in small new periodic structures in different isolations. As the pulse energy increased, the coupling between the incident beam and the surface plasmon was converted from non-resonance to resonance, thereby generating

effective coupling, and in the process, a deeper periodic structure was produced, that was, the LIPSS structure.

We have statistically and compared the relationship between the period of the material surface and the energy density under each parameter, and plotted it as Fig.6. The period of the micro-nano structure gradually increased with the increase of the energy density, but the magnitude of the change was relatively small. The period of LIPSS increased from the lowest of about 700nm (40 kHz, 0.06 J/cm^2) to the highest of 928 nm (10 kHz, 0.16 J/cm^2), which was higher than half the wavelength and smaller than the wavelength of the laser 1030 nm, which was a typical LSFL structure. When the repetition rate was 30 kHz and 40 kHz, the SWPSS structure was formed when the energy density exceeded 0.10 J/cm^2. The performance of this structure in this experiment was that the period of about 1.5 wavelengths develops with the increase of energy density to a period width of about 2 times the wavelength.

To further analyze the structure of the surface, we used a confocal microscope to further observe the surface of the material. In this analysis, a repetition rate of 30 kHz was selected to observe the effect of different energy densities on the surface of the material. Fig.7 was the contour line of the material surface, the cross-sectional direction was perpendicular to the LIPSS structure direction to facilitate the observation of the undulation of the material surface. For Fig.7A, when the energy density was 0.06 J/cm^2, due to the higher repetition rate, the surface of the material was covered with a layer of uneven LIPSS structure. Due to the low energy, there may be uniform LIPSS only near the center of the spot, while the others were mostly broad peaks with small fluctuations on the surface of the peaks. When the energy density increased to 0.10 J/cm^2, as shown in Fig.7C, the uniform LIPSS structure was distributed on the surface of the material. There were wider peaks but less distribution at the edge of the spot, and the other peak-to-valley spacing tended to be stable, and the periodicity was obvious. When the energy density continued to increase, increasing to above 0.12 J/cm^2, an SWPSS structure appeared on the surface of the material, and the cross-sectional direction was parallel to the SWPSS. We found that most areas can still maintain the characteristics of LIPSS, that was, regular peak-to-valley spacing and a period with an approximate width. But when the energy reaches 0.14 J/cm^2, the coverage area of SWPSS increased, and the LIPSS fluctuations on the cross-section of the material disappear.
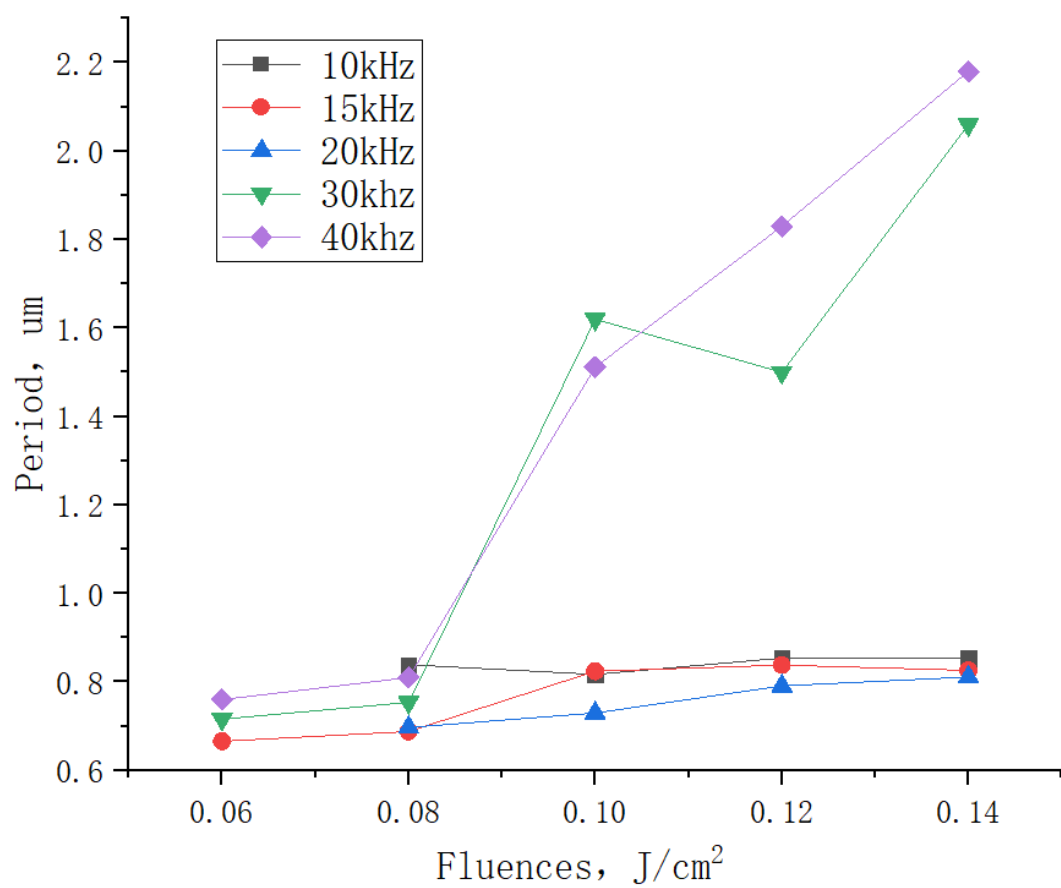
Fig.6 The relationship between energy density and texture period at different frequencies
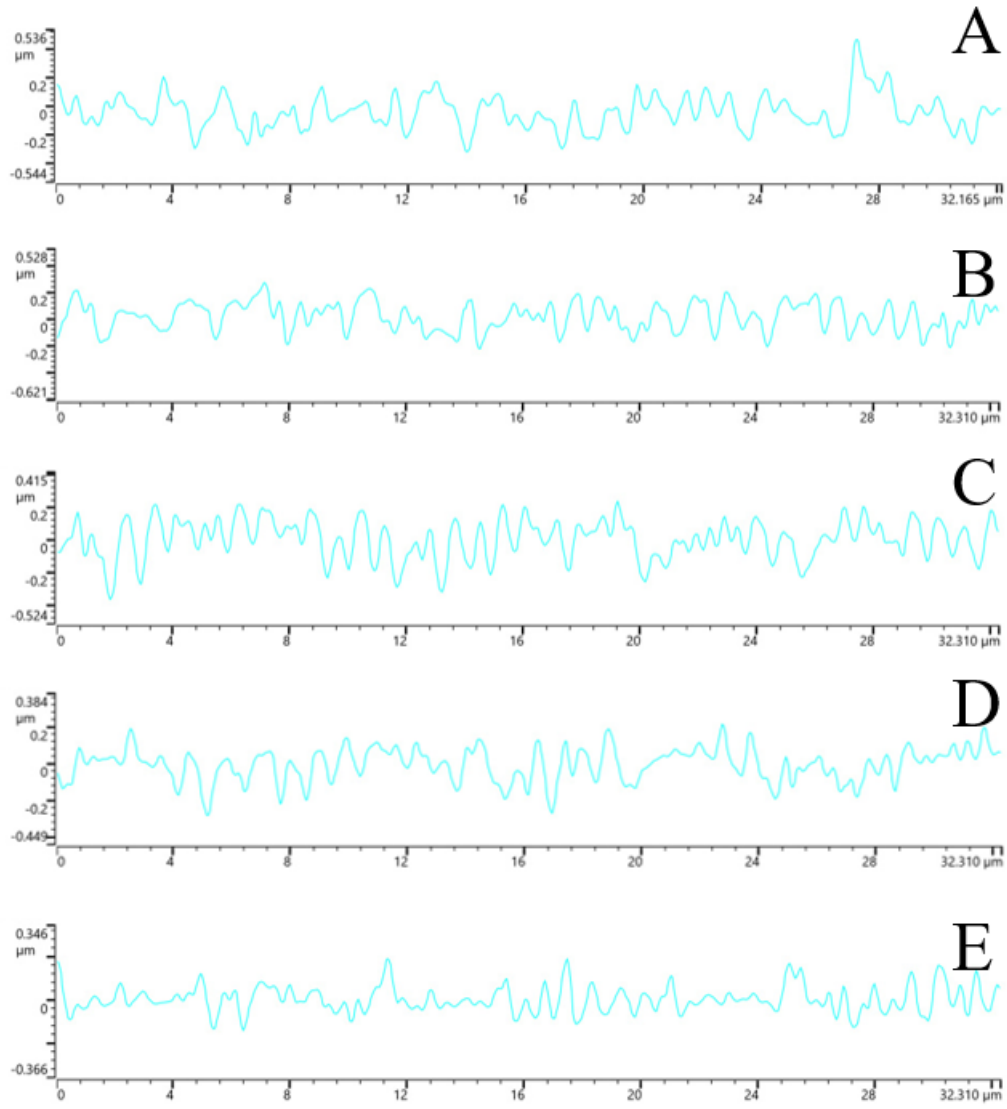
Fig.7 Confocal cross-sectional profile diagrams of the material surface under different energy densities when the repetition rate was 30 kHz. The energy density of A was 0.06 J/cm^2; the energy density of B was 0.08 J/cm^2; the energy density of C was 0.10 J/cm^2; the energy density of D was 0.12 J/cm^2; the energy density of E was 0.14 J/cm^2;

3.3　The influence of repetition rate

Laser repetition rate or repetition rate Laser pulse repetition rate was defined as the number of pulses output per second. Under the premise that the pulse width of the laser remains unchanged, a higher repetition rate means that the proportion of time that light was emitted per unit time was longer, and the proportion of time that light was not emitted was shorter. Under the premise of the same laser pulse width, a higher repetition rate means that the time ratio of light

in a unit time was longer, and the time ratio of light off was shorter. If the repetition rate was high enough, a continuous wave (CW) laser can be generated instead of a pulsed laser, and continuous light can be achieved. As the laser ablation mechanism changes from non-thermal ablation to thermal ablation. The reduction of the time for light off results in the shortening of the heat dissipation time after laser irradiation and the increase of the heat accumulation effect, thereby increasing the ablation rate.

The repetition rate was also one of the factors that affect the ablation rate. Due to the decrease of the ablation rate, the number of pulses increased with the increase of NOP and the threshold. The term incubation effect was used to describe the correlation between the ablation threshold and NOP, where the ablation threshold decreased exponentially with the increase of NOP until it reached an asymptotic value. This phenomenon can be observed in both metallic materials and polymers. In metals, this phenomenon was believed to be caused by the degradation of material properties formed by plastic stress-strain.

The effective pulse number N_{eff} experienced at the same position can be expressed as:

$$N_{\text{eff}} = \frac{2\omega_0 \text{fk}}{v} \qquad （1）$$

Where v was the scanning speed, ω_0 was the spot radius of 0.0125 mm, k was the number of elements, and f was the repetition rate .

Incubation effect formula:

$$\text{F}_{\text{th}}(\text{N}) = \text{F}_{\text{th}}(1)N^{s-1} \qquad （2）$$

Where $\text{F}_{\text{th}}(\text{N})$ was the ablation threshold of the material at the Nth pulse, $\text{F}_{\text{th}}(1)$ was the ablation threshold of the material under a single pulse, and N was the number of pulses.

For the energy density of 0.12 J/cm^2, it was a typical LIPSS structure at 10 KHz. In the process of gradually increasing the repetition rate to 20 kHz, a dot-net structure appeared, and the proportion of the dot-net structure gradually increased. The law of the process of this change was similar to that of changing the energy density, but the difference was that the principle of the change of the structure caused by the change of repetition rate was different from the change of energy density. More pulses not only bring more energy and shorter heat dissipation time but also high repetition rate can cause incubation effects. The increasing number of effective pulses will cause the incubation effect and decrease the actual ablation threshold of the material. This

phenomenon was related to laser-induced surface defects. This makes the ablation threshold of the material decrease as the repetition rate increased, and further allows the material to obtain a stronger etching effect under the same energy density. At the same time, after the previous pulse changes the shape of the material itself, the subsequent pulses irradiate the surface. Because the previous pulse forms a contour on the surface, the flatness of the surface was destroyed, so the spatial symmetry of the laser was broken. The coupling between the electric field of the incident beam and surface plasmon polaritons (SPPs) produces an uneven and periodic distribution of absorbed energy.

When the repetition rate rises and exceeds 30 kHz, the structure has a significant change(As shown in Fig.4): the structure dominated by LIPSS disappears and was replaced by a larger striped SWPSS structure parallel to the polarization direction. The characteristic of this structure was that the period was close to twice the laser wavelength. The original LIPSS structure was squeezed in the gap of the SWPSS and combined with the SWPSS to form a point hole structure in the gap. However, this structure tends to disappear as the repetition rate increased. There are many opinions about the formation of SWPSS. It was a complicated process related to the excitation mechanism of optics, heat transfer, and surface plasmon wave (SPWS). In the model constructed by E. Allahyari et al., when N_{eff}=1 and the energy were higher than the ablation threshold, the laser will form a pit on the surface of the material and produce a certain number of irregular protrusions. When N_{eff}>1, the spatial symmetry of the laser energy distribution was broken and the energy absorption mode changes, which in turn causes the material to absorb energy unevenly and has a certain periodicity. The coupling of the laser's electric field and surface protons was also one of the reasons for this phenomenon.

When the depth of the laser-induced self-organized micro/nanostructure on the surface was further increased and reached a certain threshold, the coupling will occur, which will further excite the surface plasmids and become the driving force behind the induced surface profile. When the surface profile reaches a certain scale, the thermal capillary wave that causes the normal LIPSS shape will not be generated. The hydrothermal wave propagates between the corrugated traps in a direction perpendicular to the polarization of the laser beam. The theoretical model established by George D. Tsibidis et al.: The energy of the laser causes the local material to be removed due to overheating and produces an impulse force on the surface of the material. At the same time,

uneven heat distribution and changes in surface tension cause Marangoni-driven flow and capillary waves, which ultimately lead to the formation of ablation marks and ripples, and surface tension produces protrusions near the periphery of the point. When the temperature difference inside the melt exceeds a critical value, the convective volume and hydrothermal waves generated by the surface tension gradient will induce surface traction perpendicular to the corrugation direction. The height of the corrugation decreases with the increase of N_{eff}. This was because the capillary wave amplitude is gradually suppressed due to the increase in the volume of the rising molten material. With the increase of N_{eff}, the degree of ablation and the deepening of surface texture depth, energy deposition, and temperature gradient will be intensified, which in turn promotes the formation of SWPSS.

Similarly, we have statistically and compared the relationship between the period of the material surface and the repetition rate of the laser pulse under each parameter, and plotted it as Fig.8. When the pulse repetition rate was 10 kHz, the period under each energy density will be slightly higher than that at 15 kHz, and then there was a trend that the period increased with the energy density, and at some higher energy densities, the SWPSS structure appears when the repetition rate exceeds 20 kHz. The SWPSS structure will also evolve as the repetition rate increased, from a period of 1.5 times the wavelength to a structure of 2 times the wavelength period.
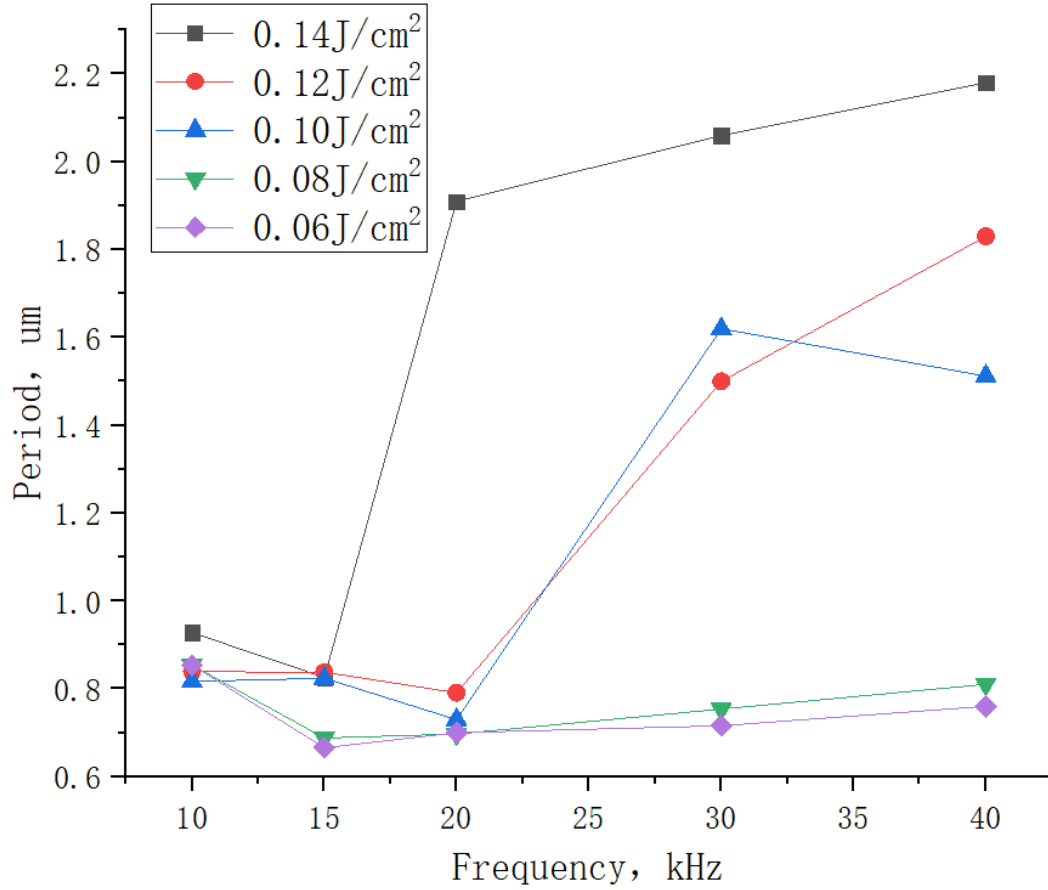
Fig.8 The relationship between repetition rate and texture period under different energy densities

To further study the influence of repetition rate on the structure of the material surface, we used a confocal microscope to observe the material surface. Fig.9 was a cross-sectional view of the material surface when the energy density was 0.08 J/cm². The interception method was the direction perpendicular to the surface structure of the material as above. Figure a shows the surface profile with a repetition rate of 10 kHz. Since the heat source follows the energy distribution of Gaussian light, the position where the material fluctuates greatly was the center of the pulse. A small and inconspicuous stripe structure was formed inside, which was very shallow and relatively rare. There are obvious slight fluctuations in other positions, which are foreshadowing the subsequent coupling of surface plasmons and incident laser beams. In Fig.9B, the repetition rate was increased to 15 kHz. As the number of pulses increased, the depth of the ripple increased significantly. The uniform LIPSS structure was still only distributed in the center of the spot, but the range was larger than that of Fig.9A, and the same was true for Fig.9C. In Fig.9D,

LIPSS has covered the surface of the material and the peak-to-valley gap was relatively uniform, but at the center of the light spot, the surface of the material has the characteristic of overall depression. When the repetition rate was further increased to 40 kHz, as shown in Fig.9D because the structure of the material surface changes from LIPSS to a dot mesh structure, the contour lines are relatively messy, and some adjacent peaks are connected to form a new broad peak.
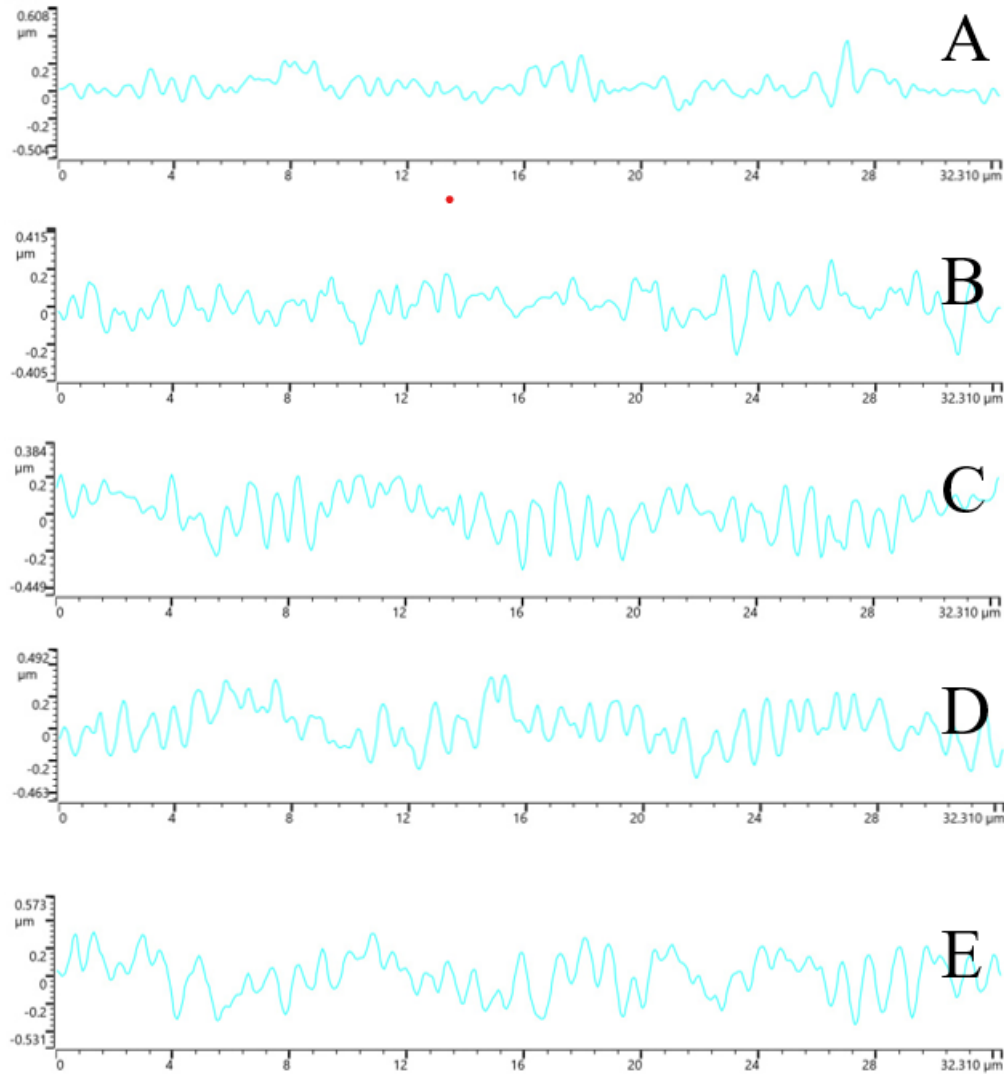

Fig.9 Confocal cross-sectional profiles of the material surface at different frequencies when the energy density was 0.08 J/cm^2 The repetition rate of A was 10 kHz; the repetition rate of B was 15 kHz; the repetition rate of C was 20 kHz; the repetition rate of D was 30 kHz; the repetition rate of E was 40 kHz;

4. Summary

In this paper, a femtosecond laser was used to process the $Zr_{64.13}Cu_{15.75}Ni_{10.12}Al_{10}$ amorphous

alloy, and the formation of the self-organized micro-nano structure from the laser to the surface was studied. Explained its formation mechanism and the influence of different experimental parameters (such as repetition rate , energy density, scanning speed, etc.) on the surface texture, and studied the point ablation and surface ablation, and described the experimental results in detail. The results of the study are as follows:

1. The increase in the number of effective pulses will cause the incubation effect, which will significantly reduce the ablation threshold of the material. This will affect the changes in the surface morphology of the material.

2. The increase in the number of pulses will enlarge the diameter of the affected zone of point ablation, but too many pulses will damage the core structure due to excessive heat energy.

3. In a suitable interval, the increase of energy density will gradually clear and deepen the structure of LIPSS. When the repetition rate exceeds a certain value, the higher energy density will make the LIPSS gradually change to the SWPSS structure.

4. The incubation effect allows the repetition rate to affect the formation of the surface texture of the material when processing the surface of the material. While deepening the peak and valley value of the texture, it will also make the LIPSS transform to the SWPSS texture.

5. Comparing the number of bacteria adsorbed by the smooth surface and the LIPSS surface in the Staphylococcus aureus culture solution, the LIPSS structure can effectively reduce the adsorption of Staphylococcus aureus, indicating that this structure has a good antibacterial ability.

Reference

[1]   Ibrahim MZ, Sarhan AAD, Kuo TY, Yusof F, Hamdi M. Characterization and hardness enhancement of amorphous Fe-based metallic glass laser cladded on nickel-free stainless steel for biomedical implant application. Mater Chem Phys 2019;235:121745. https://doi.org/10.1016/j.matchemphys.2019.121745.

[2]   Lei Y, Zhang N, Yang J, Guo C. Femtosecond laser eraser for controllable removing periodic microstructures on Fe-based metallic glass surfaces. Opt Express 2018. https://doi.org/10.1364/oe.26.005102.

[3]   Liu L, Liu Z, Chan KC, Luo HH, Cai QZ, Zhang SM. Surface modification and biocompatibility of Ni-free Zr-based bulk metallic glass. Scr Mater 2008. https://doi.org/10.1016/j.scriptamat.2007.09.040.

[4]   Lei Y, Zhang N, Yang J, Guo C. Femtosecond laser eraser for controllable removing periodic microstructures on Fe-based metallic glass surfaces. Opt Express 2018;26:5102. https://doi.org/10.1364/OE.26.005102.

[5]   Allahyari E, JJ Nivas J, Skoulas E, Bruzzese R, Tsibidis GD, Stratakis E, et al. On the formation and features of the supra-wavelength grooves generated during femtosecond laser surface structuring of silicon. Appl Surf Sci 2020;528:146607. https://doi.org/10.1016/j.apsusc.2020.146607.

[6]   Ida H, Seiryu M, Takeshita N, Iwasaki M, Yokoyama Y, Tsutsumi Y, et al. Biosafety, stability, and osteogenic activity of novel implants made of Zr70Ni16Cu6Al8 bulk metallic glass for biomedical application. Acta Biomater 2018;74:505–17. https://doi.org/10.1016/j.actbio.2018.05.020.

[7]   Zhu Y, Fu J, Zheng C, Ji Z. Effect of nanosecond pulse laser ablation on the surface morphology of Zr-based metallic glass. Opt Laser Technol 2016;83:21–7. https://doi.org/10.1016/j.optlastec.2016.03.021.

[8]   Shrikant S. Non-Isothermal Laser Treatment of Fe-Si-B Metallic Glass 2017.

[9]   Qiu CL, Chen Q, Liu L, Chan KC, Zhou JX, Chen PP, et al. A novel Ni-free Zr-based bulk metallic glass with enhanced plasticity and good biocompatibility. Scr Mater 2006;55:605–8. https://doi.org/10.1016/j.scriptamat.2006.06.018.

[10] Irizawa A, Suga S, Nagashima T, Higashiya A, Hashida M, Sakabe S. Laser-induced fine structures on silicon exposed to THz-FEL. Appl Phys Lett 2017;111. https://doi.org/10.1063/1.5006014.

[11] Schwarz S, Rung S, Hellmann R. High Quality One-Dimensional Low Spatial Frequency Lipss on Sapphire Generated by Top-hat Beam Shaped Ultrashort-Pulsed Laser 2018:11–3.

https://doi.org/10.26649/musci.2017.019.

[12] Huang H, Jiang M, Yan J. The coupling effects of laser thermal shock and surface nitridation on mechanical properties of Zr-based metallic glass. J Alloys Compd 2019;770:864–74. https://doi.org/10.1016/j.jallcom.2018.08.195.

[13] Huang L, Cao Z, Meyer HM, Liaw PK, Garlea E, Dunlap JR, et al. Responses of bone-forming cells on pre-immersed Zr-based bulk metallic glasses: Effects of composition and roughness. Acta Biomater 2011. https://doi.org/10.1016/j.actbio.2010.08.002.

[14] Gaggl A, Schultes G, Müller WD, Kärcher H. Scanning electron microscopical analysis of laser-treated titanium implant surfaces-a comparative study. Biomaterials 2000. https://doi.org/10.1016/S0142-9612(00)00002-8.

[15] Jorge-Mora A, Imaz N, Garcia-Lecina E, O'Connor GM, Gómez-Vaamonde R, Alonso-Pérez A, et al. In vitro response of bone marrow mesenchymal stem cells (hBMSCs) on laser-induced periodic surface structures for hard tissue replacement: Comparison between tantalum and titanium. Opt Lasers Eng 2018;111:34–41. https://doi.org/10.1016/j.optlaseng.2018.07.008.

[16] Sergiienko RA, Shcheretskyi OA, Zadorozhnyy VY, Verkhovliuk AM, Louzguine-Luzgin D V. Investigation of Zr55Cu30Al10Ni5 bulk amorphous alloy crystallization. J Alloys Compd 2019;791:477–82. https://doi.org/10.1016/j.jallcom.2019.03.270.

[17] Tsibidis GD, Fotakis C, Stratakis E. From ripples to spikes: A hydrodynamical mechanism to interpret femtosecond laser-induced self-assembled structures. Phys Rev B - Condens Matter Mater Phys 2015;92:1–6. https://doi.org/10.1103/PhysRevB.92.041405.

[18] Li C, Zhang H, Cheng G, Faure N, Jamon D, Colombier JP, et al. Initial cumulative effects in femtosecond pulsed laser-induced periodic surface structures on bulk metallic glasses. J Laser Micro Nanoeng 2016;11:357–65. https://doi.org/10.2961/jlmn.2016.03.0014.